

Intermetallics Based on Sodium Chalcogenides Promote Stable Electrodeposition–Electrodissolution of Sodium Metal Anodes

Yixian Wang,* Hui Dong, Naman Katyal, Bairav S. Vishnugopi, Manish K. Singh, Hongchang Hao, Yijie Liu, Pengcheng Liu, Partha P. Mukherjee, Graeme Henkelman, John Watt, and David Mitlin*

Sodiophilic micro-composite films of sodium-chalcogenide intermetallics (Na_2Te and Na_2S) and Cu particles are fabricated onto commercial copper foam current collectors ($\text{Na}_2\text{Te}@CF$ and $\text{Na}_2\text{S}@CF$). For the first time a controllable capacity thermal infusion process is demonstrated. Enhanced wetting by the metal electrodeposition leads to state-of-the-art electrochemical performance. For example, $\text{Na}_2\text{Te}@CF$ -based half-cells demonstrate stable cycling at 6 mA cm^{-2} and 6 mAh cm^{-2} , corresponding to $54 \mu\text{m}$ of Na electrodeposited/electrodissolved by geometric area. Sodium metal batteries with $\text{Na}_3\text{V}_2(\text{PO}_4)_3$ cathodes are stable at 30C (7 mA cm^{-2}) and for 10 000 cycles at 5C and 10C. Cross-sectional cryogenic focused ion beam (cryo-FIB) microscopy details deposited and remnant dissolved microstructures. Sodium metal electrodeposition onto $\text{Na}_2\text{Te}@CF$ is dense, smooth, and free of dendrites or pores. On unmodified copper foam, sodium grows in a filament-like manner, not requiring cycling to achieve this geometry. Substrate–metal interaction critically affects the metal–electrolyte interface, namely the thickness and morphology of the solid electrolyte interphase. Density functional theory and mesoscale simulations provide insight into support-atom energetics, nucleation response, and early-stage morphological evolution. On Na_2Te sodium atomic dispersion is thermodynamically more stable than isolated clusters, leading to conformal atom coverage of the surface.

1. Introduction

The past 3 decades have witnessed the dominance of lithium-ion batteries (LIBs), with extensive applications ranging from portable electronics to electric vehicles. However as demand for LIBs continues to grow, concerns are raised regarding the economic and supply-chain sustainability of key elements making up the cathode, including Li precursors, Co and Ni.^[1–3] Sodium-based secondary batteries are emerging as potential alternatives to LIBs due to their analogous working mechanism but the greater availability of sodium precursors and the other elements making up the cathode.^[4–11] Especially for stationary medium-range and long-range applications, such as grid backup, sodium-based batteries are a viable competitor due to their reduced cost in terms of dollars per kilowatt hour.^[12–16] Having both sodium and lithium-based energy storage available also serves as a hedge against intermittently spiking LIB costs as their price is highly sensitive to marginal demand.^[17–21] Secondary

sodium-based batteries may be classified analogously to lithium-based batteries. A sodium-ion battery (NIB, SIB) is based on an ion insertion anode such as hard carbon, with a useful capacity of $\approx 300 \text{ mAh g}^{-1}$. Numerous sodium-focused efforts have been devoted to developing suitable electrode materials for SIBs with larger capacity, higher output voltage, and greater specific energy.^[22–26]

A sodium metal battery (SMB) is based on a metallic electrodeposition/electrodissolution anode, with a theoretical capacity of 1165 mAh g^{-1} . SMBs hold considerable promise due to the high theoretical capacity of the metal anode and the associated low electrodeposition/electrodissolution potential ($0.33 \text{ V vs Li/Li}^+$).^[27–32] Unfortunately, the metal dendrite growth and the associated unstable solid electrolyte interphase (SEI) prevail with SMBs in a wide range of electrolytes.^[33–37] The continuous volume fluctuation and morphology change during electrodeposition/electrodissolution associated with hostless Na lead to deteriorated SEI and intensified local current density, aggravating dendrite growth and electrolyte depletion.^[38–42]

Y. Wang, H. Dong, H. Hao, Y. Liu, P. Liu, D. Mitlin
Materials Science and Engineering Program and Texas Materials Institute (TMI)

The University of Texas at Austin
Austin, TX 78712, USA

E-mail: yixwang@utexas.edu; david.mitlin@austin.utexas.edu

N. Katyal, G. Henkelman

Department of Chemistry

The University of Texas at Austin
Austin, TX 78712, USA

B. S. Vishnugopi, P. P. Mukherjee

School of Mechanical Engineering

Purdue University

West Lafayette, IN 47907, USA

M. K. Singh, J. Watt

Center for Integrated Nanotechnologies

Los Alamos National Laboratory

Los Alamos, NM 87545, USA

 The ORCID identification number(s) for the author(s) of this article can be found under <https://doi.org/10.1002/aenm.202204402>

DOI: 10.1002/aenm.202204402

Various solutions have been put forth to address this interlinked dendrite–SEI problem.^[43–45] One set of effective approaches involves the formation of a surface passivation layer with enhanced electrochemical stability. This has been achieved through electrolyte additives such as KFSl,^[46] SnCl₂,^[47] SbF₃,^[48] and Na₂S₆,^[49] or by fabrication of an “artificial SEI” through surface coatings such as Al₂O₃,^[50,51] NaBr,^[52] NaI,^[53] Na/Bi,^[54] and Na/Sb^[55] alloys. Another effective approach is based on metallic layers that reversibly alloy and dealloy with the Na at every cycle. Reversible alloying anodes such as Na–Ge, Na–Sn, Na–Sb, and Na–Au have been shown to be effective with SMBs that employ relatively thick sodium metal anodes to serve as an ion reservoir during full cell cycling.^[47,56–60] Yu’s group created Na₂Te-based anode protection layers by directly painting nanosized Te powder onto the sodium-metal surface, achieving state-of-the-art electrochemical performance.^[28] These modifications were aimed at creating an artificial SEI layer, and did not affect the current collector structure or surface chemistry.

Another approach is based on the enhanced surface area of the current collector, such as with 3D metal foams rather than with 2D foils, which reduces the current density per unit area of the anode. Per Sand’s model^[61,62] the reduced current density allows for higher C-rate performance before the onset of concentration polarization–driven dendrite growth. When nucleation occurs on the entire surface of a 3D support there is also a geometric impediment to the dendrites growing directly toward the separator, as their growth directions will vary with the substrate geometry. 3D supports have been reported to refine the electrodeposition growth front, with a greater number of initial metal nuclei and correspondingly smaller crystalline size.^[63,64] Designing sodiophilic substrates to enhance Na wetting during electrodeposition and simultaneously decrease the nucleation/growth overpotentials has been demonstrated to be an efficient strategy for enhanced electrochemical performance.^[65–74] For example, authors prepared a NiSb-coated current collector using a galvanic displacement reaction, promoting smooth electrodeposition of Na metal.^[17] Researchers employed SnO₂ quantum dots to transform a sodiophobic carbon cloth into a sodiophilic surface, allowing for stabilized deposition and suppressed dendrite growth.^[75] Zhang et al. fabricated high-performance Na–Na₂S–carbon hybrid anodes by immersing S-doped carbon paper into molten sodium, employing tissue paper as the carbon precursor.^[76] Other novel surface-modified structures that significantly enhanced electrochemical performance include Cu₂O nanowires on Cu foam,^[77] MXene–rGO membranes,^[78] and heteroatom-doped carbon nanofibers.^[76,79]

In this study it is demonstrated a thin surface layer of electrochemically stable intermetallics (two systems examined, Na₂Te and Na₂S) thermally deposited onto a commercial 3D copper foam (CF) current collector enables state-of-the-art SMB electrochemical performance. The key difference observed versus the uncoated baseline copper foam is the wetting behavior of the sodium, which appears to have a major influence on almost all aspects of the electrodeposition/electrodissolution process, including overpotentials, Coulombic efficiency (CE), dendrite growth, and SEI formation. The Na₂Te/Na₂S systems were selected based on the known electrochemical properties of these materials as functional SMB cathodes. At metal anode electrodeposition/electrodissolution voltages, both intermetallics are kineti-

cally stable once formed, not undergoing additional conversion reactions during cycling. Meanwhile the remnant Cu particles densely interspersed with the intermetallics (Cu₂Te/Cu₂S + 2Na⁺ + 2e[−] → Na₂Te/Na₂S + 2Cu) allow for the coated current collectors to remain electrically conductive. The kinetic electrochemical stability of the Na₂Te/Na₂S is the key to the proposed strategy. The stable sodiophilic intermetallic methodology is different from applying alloying layer approaches that have been extensively studied to promote electrodeposition/electrodissolution, where significant volume changes occur at every cycle.^[27,32,80] From both metal battery and ion battery literature, it is known that repeated volume changes at the anode promote ongoing and often unstable SEI growth.^[68,69,81] By contrast, the kinetically stable Na₂Te/Na₂S intermetallic eliminates such volumetric expansion–contraction at every cycle. It is demonstrated that more favorable electrochemical performance is achieved with Na₂Te rather than with Na₂S, likely due to better coating integrity of the telluride.

2. Results and Discussion

The sodium chalcogenides and Cu particles coated 3D copper foam (CF) current collectors were fabricated using a one-step heat-treatment method, summarized below. The initial surface area of the foam was ≈3 m² kg^{−1} (provided by the vendor) and would not change due to it being mechanically compressed. The cleaned commercial copper foam (CF) was first cut and pressed to a thickness of 360 μm by a hydraulic press. It was then mounted at the top of an alumina crucible with a fixed amount of Te or S powder on the bottom and transferred to a tube furnace. The thermal treatment was performed at 600 °C for 1 h in an argon atmosphere. The evaporated Te/S reacts with Cu to form a homogeneous layer of copper telluride (Cu₂Te) and copper sulfide (Cu₂S) intermetallics. For the two systems the geometric area mass loadings were 1.6 and 1.2 mg cm^{−2}, respectively. Figure S1, Supporting Information, provides a schematic top-down view of the as-fabricated substrates. The obtained structures were not yet in situ reacted with Na ions to yield the targeted Na₂Te and Na₂S intermetallics and are therefore labeled “S@CF” and “Te@CF.” Figure S2a–c, Supporting Information, presents digital photographs showing the thickness of CF, as well as the front and the back sides of CF, S@CF, and Te@CF. Since thermal evaporation is a line-of-sight process, the back-facing side of the foams remained almost unchanged, as confirmed by optical inspection. For practical applications, a double-side treated CF may be achieved by turning the compressed foam over and repeating the evaporation process.

Figure S3a–f, Supporting Information, presents SEM images at different magnifications of the as-fabricated specimens. Figure S3a,b, Supporting Information, presents the baseline copper foam (CF). Figure S3c,d, Supporting Information, presents the results for Te@CF while Figure S3e,f, Supporting Information, presents the results for S@CF. Figure S3g, Supporting Information, compares the XRD profiles of Te@CF, S@CF, and CF. Figure S3h,i, Supporting Information, shows the high-resolution XPS spectra of Cu 2p and Te 3d of Te@CF, with analogous XPS results for Te@CF being shown in Figure S9, Supporting Information. As shown in Figure S3a–f, Supporting Information, the originally smooth and glossy surface of CF becomes covered with

micro-scale platelets of Cu_2Te with a typical thickness of 200 nm. The morphology of S@CF is that of interconnected globular rods with a typical diameter in the 4 μm range. Figure S4, Supporting Information, shows energy dispersive X-ray spectroscopy (EDXS) maps and the spectrum of Te@CF indicating that the distribution of Te is relatively uniform throughout the copper surface. Figure S5, Supporting Information, presents EDXS analysis performed on S@CF likewise indicating a relatively uniform coating of the element. Since the foam was not planar and thermal evaporation is a line-of-sight process, the coatings were not entirely homogeneous. Some of the observed signal intensity variation is also caused by the geometry of the compressed foam per se. The 3D geometry and its orientation relative to the electron beam will give differences in signal intensity even if the Te or S layers were completely uniform.

X-ray diffraction (XRD) measurements were carried out to analyze the structure of the coatings, the results being shown in Figure S3g, Supporting Information. The baseline commercial CF is fcc ($a = 0.3613$ nm) with space group Fm-3m and three characteristic peaks at 43.3° , 50.4° , and 74.1° belonging to the (111), (200), (220) planes. After Te treatment, four additional peaks at 12.1° , 24.4° , 27.2° , and 44.8° are observed, corresponding to the hcp ($a = 0.4237$ nm, $c = 0.7274$ nm) Cu_2Te structure with space group P6/mmm. No characteristic peaks of elemental Te were detected, indicating complete reaction of Te with the CF.^[82] Figure S6, Supporting Information, displays transmission electron microscopy (TEM) analysis obtained from an electron transparent portion of a Cu_2Te platelet. Figure S6a,b, Supporting Information, shows bright field images of the specimen, while Figure S6c, Supporting Information, provides a high-resolution TEM (HRTEM) image with an inset showing the associated selected area electron diffraction pattern. The HRTEM image displays well-defined lattice fringes, indicating a high degree of crystallinity in agreement with the XRD results. The same intermetallic structure was also obtained when lowering the Cu_2Te loading from 1.6 mg cm^{-2} to 0.8 and 0.2 mg cm^{-2} . As indicated by the XRD profiles shown in Figure S7, Supporting Information, there is no discernible structural difference at these lower mass loadings. Figure S8, Supporting Information, presents SEM images that display the morphologies of the coatings with the lower Te loading. A similar plate-like structure is present at both loadings, although the number density of the plates decreases at 0.2 mg cm^{-2} . The specimen with the mass loading of 1.6 mg cm^{-2} displayed the best electrochemical performance and was therefore selected for the detailed analytical studies. However, the lower Cu_2Te loadings also led to substantial improvements over the uncoated baseline. Lower mass loading coatings were not fabricated for Cu_2S .

X-ray photoelectron spectroscopy (XPS) was conducted to study the surface chemistry of Te@CF . Figure S3h, Supporting Information, shows the high-resolution Cu 2p spectrum. The peaks at 931.8 and 951.5 eV are assigned to Cu^0/Cu^+ $2p_{3/2}$ and Cu^0/Cu^+ $2p_{1/2}$ while the peaks at 932.5 and 952.2 eV are ascribed to Cu^{2+} $2p_{3/2}$ and Cu^{2+} $2p_{1/2}$. Per Figure S3i, Supporting Information, there is one pair of peaks in the high-resolution Te 3d spectrum, which corresponds to the Te^{2-} $3d_{5/2}$ at 572.4 eV and Te^{2-} $3d_{3/2}$ at 582.8 eV, respectively. These results further confirm that no elemental Te remains on the surface. The structure and surface chemistry of S@CF were also examined using XRD and XPS. As shown in Figure S3g, Supporting Informa-

tion, the new peaks present after the sulfurization process are assigned to the monoclinic Cu_2S phase with P21/c space group (JCPDS#33-0490). Figure S9, Supporting Information, presents the high-resolution XPS spectra of Cu 2p (Figure S9a, Supporting Information) and S 2p (Figure S9b, Supporting Information) of S@CF . The peaks at 932.2 and 951.9 eV are assigned to Cu^0/Cu^+ $2p_{3/2}$ and Cu^0/Cu^+ $2p_{1/2}$ while the peaks at 932.9 and 952.6 eV are assigned to Cu^{2+} $2p_{3/2}$ and Cu^{2+} $2p_{1/2}$. The peaks at 161.7 and 162.9 eV are ascribed to the S^{2-} $2p_{3/2}$ and S^{2-} $2p_{1/2}$, respectively. These findings confirm the formation of Cu_2S and the absence of unreacted S on the CF surface.

Electrochemical measurements were carried out using a two-electrode configuration in CR2032 coin cells. For half-cells, the copper foams were used as the working electrodes while Na metal was employed as the reference and counter electrode. Two types of electrolytes were employed including 1 M NaPF_6 in dG2 and 1 M NaClO_4 in EC:PC (1:1 by volume) with 10 wt% FEC. The ether-based electrolyte was mainly used for electrochemical tests unless otherwise mentioned. Two pieces of tri-layer polypropylene/polyethylene/polypropylene (Celgard 2325) or one piece of glass fiber (Whatman GF/D) were used as the separator in ether and carbonate-based electrolytes, respectively. In situ electrochemical sodium activation of the $\text{Cu}_2\text{Te}/\text{Cu}_2\text{S}$ intermetallic was employed to fabricate the final $\text{Na}_2\text{Te}/\text{Na}_2\text{S}$ intermetallic-Cu particle sodiophilic layer on the Cu foam surface, namely $\text{Na}_2\text{Te@CF}$ and $\text{Na}_2\text{S@CF}$. The activation process consists of cycling the half-cells between 0 to 1 V at 0.1 mA cm^{-2} for five cycles, being performed prior to the electrodeposition/electrodissolution studies. The formation of sodium chalcogenides of $\text{Na}_2\text{Te}/\text{Na}_2\text{S}$ is nonreversible under the experimental test conditions, indicating there is no extra Na reservoir on the activated collector.

Figure 1 presents the electrochemical signatures, and morphological and structural changes during the in situ activation process. Figure 1a,b displays the first five consecutive galvanostatic discharge/charge profiles of Te@CF and S@CF substrates for sodium activation, tested within 0–1 V at 0.1 mA cm^{-2} . Figure 1c–f provides different magnification SEM images of $\text{Na}_2\text{Te@CF}$ and $\text{Na}_2\text{S@CF}$ after activation. Figure 1g shows the XRD profiles of $\text{Na}_2\text{Te@CF}$ and $\text{Na}_2\text{S@CF}$. Figure 1h,i shows the high-resolution XPS spectra of Cu 2p and Te 3d of $\text{Na}_2\text{Te@CF}$, with analogous XPS results for $\text{Na}_2\text{S@CF}$ being shown in Figure S12, Supporting Information. The activation process is an irreversible conversion reaction at cycle 1 (at a maximum anodic voltage of 1 V), where the $\text{Cu}_2\text{Te}/\text{Cu}_2\text{S}$ layers react with Na form $\text{Na}_2\text{Te}/\text{Na}_2\text{S}$ and Cu. For $\text{Cu}_2\text{Te} + 2\text{Na}^+ + 2\text{e}^- \rightarrow \text{Na}_2\text{Te} + 2\text{Cu}$ there is a distinct sodiation plateau at 1.1 V, which is not reversed at desodiation. For $\text{Cu}_2\text{S} + 2\text{Na}^+ + 2\text{e}^- \rightarrow \text{Na}_2\text{S} + 2\text{Cu}$, there are two sloping plateaus corresponding to stepwise sodiation through intermediate solid-state products such as Na_2S_2 .^[83–88] During the first desodiation to 1 V, as well as in the four subsequent cycles, both $\text{Na}_2\text{Te@CF}$ and $\text{Na}_2\text{S@CF}$ deliver negligible capacity, confirming kinetic irreversibility.

The in situ activation process was further analyzed using cyclic voltammetry (CV), at a scan rate of 0.1 mV s^{-1} and a voltage window of 0–2.5 V. As shown in Figure S10a, Supporting Information, for Te@CF the major reduction peak is centered near 0.9 V. During the anodic scan, no oxidation peak is present until 1.45 V. Per Figure S10b, Supporting Information, for S@CF the anodic peak centered near 1.55 V. Therefore, it can be safely concluded

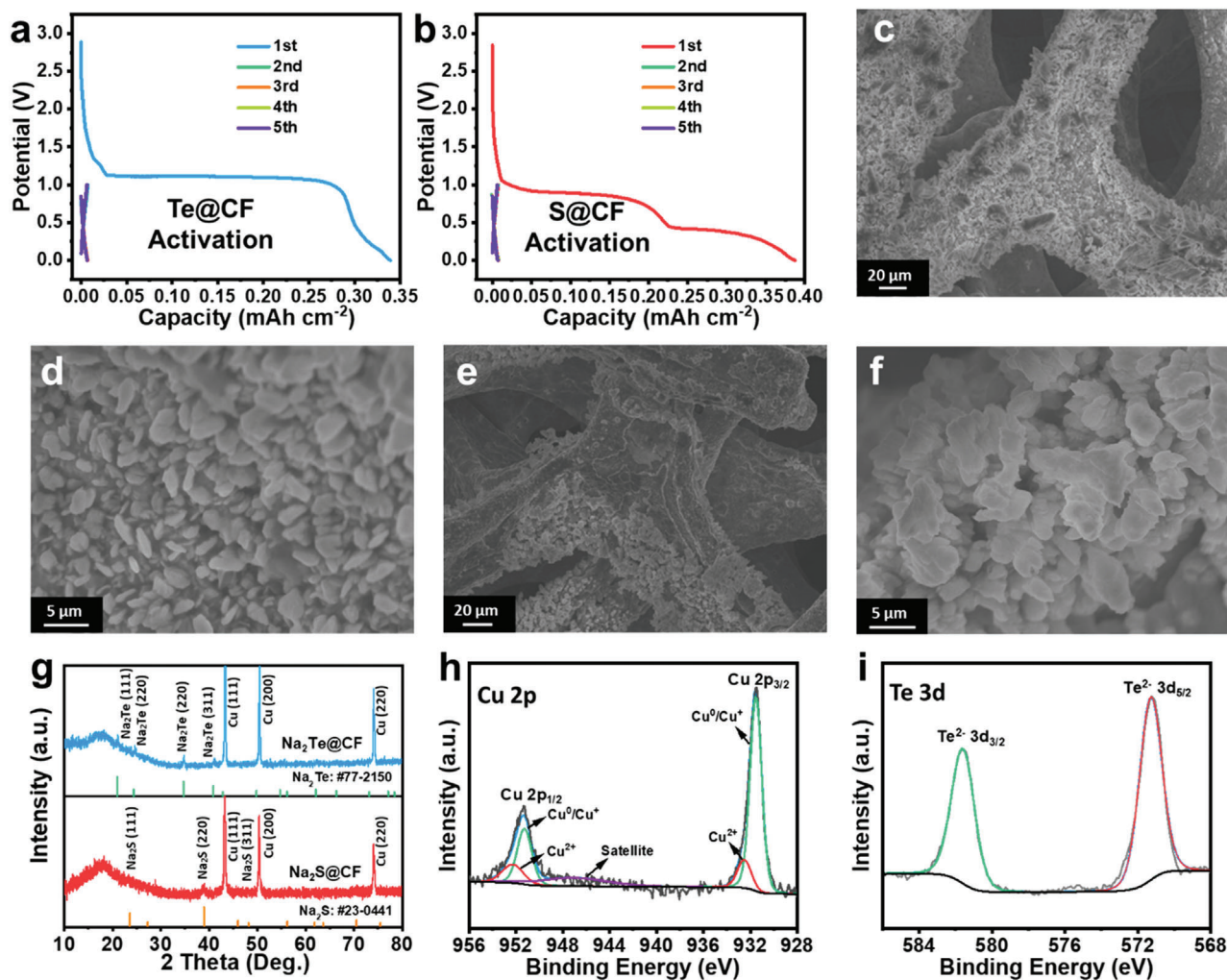


Figure 1. Electrochemical profiles, morphological, and structural changes during the in situ activation process. a,b) Galvanostatic discharge/charge curves of Te@CF and S@CF during activation. c,d) Increasing magnification SEM images of the formed Na₂Te@CF surfaces. e,f) Same analysis for Na₂S@CF. g) Indexed XRD profiles of as-fabricated Na₂Te@CF and Na₂S@CF. h,i) High-resolution XPS spectra of Cu 2p and Te 3d for Na₂Te@CF, with same analysis for Na₂S@CF shown in Supporting Information.

that neither Na₂Te nor Na₂S serves as a reversible source of Na during electrodeposition/electrodissolution experiments, either in half-cells or in full batteries. Importantly this indicates that these layers do not undergo volume changes during electrodeposition/electrodissolution of the Na metal, making them distinct from reversible alloy layers. Sodium alloy anodes such as P, Ge, Sn, and Sb will undergo reversibly dealloying at relatively low anodic voltages (≈ 0.7 V for P,^[89] ≈ 0.5 V for Ge,^[56] ≈ 0.2 V for Sn,^[57] and ≈ 0.7 V for Sb^[58,59]). By contrast, Na₂Te requires an anodic voltage of ≈ 1.5 V to achieve a reversible conversion reaction.^[90–93] With metal anodes, the upper voltage would not reach such a value either in half-cell/symmetric cell or full battery configurations. Since Na₂Te/Na₂S intermetallics do not decompose during repeated cycling, they are different from alloying supports discussed in the Introduction.

Figure 1c,d shows the SEM images of Na₂Te@CF after in situ activation. It may be observed that there is a morphology change of the coating. The CF surface becomes covered by an intercon-

nected layer of irregular shaped micron-size particles, which replace the plate-like Cu₂Te layer. The associated EDXS analysis is shown in Figure S11, Supporting Information, indicating a relatively uniform distribution Na₂Te and Cu particles throughout the surface. In this micro-scale composite architecture, the percolated Cu particles enhance electrical conductivity, making it suitable as a current collector where the Na metal electrodeposits on its surface. This is distinct from a prior study where the Na₂Te was employed an artificial SEI, with metal electrodeposition occurring underneath it.^[28] Detailed microstructural analysis of the Na metal electrodeposition morphology on top of Na₂Te@CF will be provided throughout the manuscript. Figure 1e,f shows the SEM images of Na₂S@CF after the in situ Na activation. The images highlight exposed underlying CF, indicating imperfect adherence of the Na₂S to the underlying Cu metal. This is likely one reason why this support was electrochemically inferior to Na₂Te@CF: The exposed CF regions would be poorly wetted by the Na metal electrodeposits and would likely initiate dendrite

growth during cycling. During cycling additional Cu surface may become exposed to the electrolyte as the Na₂S coating peels off further. In addition, density functional theory (DFT) analysis will demonstrate stronger work of adhesion of Na atoms on Na₂Te versus on Na₂S. A stronger work of adhesion is associated with improved wetting behavior, indicating that Na₂Te is a more sodiophilic support than Na₂S. This further explains the improved performance of Na₂Te@CF as compared to Na₂S@CF, especially the trends in the electrodeposition nucleation overpotentials, as discussed below.

Figure 1g provides the XRD profiles of Na₂Te@CF and Na₂S@CF after activation. In the diffraction patterns, the characteristic peaks associated with Cu₂Te or Cu₂S have vanished. Instead, peaks at 21.1°, 24.6°, 34.9°, and 41.1° are present being assigned to fcc antiferrofluoride Na₂Te intermetallic (JCPDS#77-2150). Similarly, peaks assigned to fcc antiferrofluoride Na₂S intermetallic (JCPDS#23-0441) are present. Figure 1h,i shows the high-resolution Cu 2p and Te 3d XPS spectra for Na₂Te@CF. It may be observed that the ratio of Cu²⁺ to Cu⁰/Cu⁺ decreases significantly as compared to the specimen analyzed in Figure S3h, Supporting Information. The Te remains in the reduced state with two peaks at 571.2 and 581.6 eV, respectively. This indicates the formation of sodium telluride and concurrent reduction of copper to its metallic state. Figure S12a,b, Supporting Information, displays the high-resolution of Cu 2p and S 2p XPS spectra of Na₂S@CF, from which a similar conclusion can be drawn regarding the formation of sodium sulfides and the reduction of copper.

Figure 2 presents the electroanalytical investigation of the Na₂Te@CF and Na₂S@CF against baseline CF supports. Figure 2a,b displays the nucleation overpotential of Na on Na₂Te@CF, Na₂S@CF, and baseline CF in half-cell configurations, tested at 0.2 and 0.5 mA cm⁻², respectively. Figure 2c,d provides the Coulombic efficiencies (CEs) during Na electrodeposition/electrodissolution at different currents and capacities. Regarding both overpotentials and CE values, while Na₂S@CF does improve the performance over the baseline, the Na₂Te@CF is more effective by a wide margin. As mentioned in the previous paragraph, this is likely related to the exposed CF regions on the Na₂S@CF surface. As shown in Figure 2a, the initial nucleation overpotentials were significantly reduced from 79 mV on bare CF to 18 mV on Na₂Te@CF and 23 mV on Na₂S@CF at a current density of 0.2 mA cm⁻². The overpotential of Na₂Te@CF also remains the lowest when the current increases to 0.5 mA cm⁻² with a value of 28 mV, in contrast to 140 mV of CF and 37 mV of Na₂S@CF. To further elucidate the role of the coatings on the electrodeposition of sodium metal, a customized electrode was fabricated with partial CF being exposed to tellurium vapor to form Cu₂Te and the other half remaining uncoated. Per Figure S13, Supporting Information, after electrodepositing 1 mAh cm⁻² Na at 0.5 mA cm⁻², the Na electrodeposit uniformly covers the Cu₂Te side, while minimal metal is deposited on the untreated CF. This provides a direct comparison between the two surface structures/chemistries in one tested electrode.

Figure S14, Supporting Information, presents a comparison of the Na electrodeposition/electrodissolution CE with the three supports. The tests were done according to an established protocol used for evaluating the efficiency of Li electrodeposition.^[94] The current density for the tests was kept at 0.5 mA cm⁻². Initially

the working electrode of the half-cell was cycled five times, electrodepositing 1 mAh cm⁻² followed by dissolving to an anodic limit of 0.5 V. This eliminated surface contaminants and stabilized the SEI. A reservoir of 5 mAh cm⁻² Na was then deposited, followed by ten cycles of electrodeposition/electrodissolution (from the reservoir) of 0.5 mAh cm⁻². Finally, the entire reservoir was dissolved to the 0.5 V anodic limit, with the CE being obtained at this step. For Na₂Te@CF, Na₂S@CF, and the baseline CF, the calculated CEs were 99.69%, 98.96%, and 97.28%, respectively. The observed difference in the CEs is attributed to a difference in the extensiveness SEI growth which is known to irreversibly consume Na ions. Another possible factor is the formation of electrochemically inactive “dead metal” on the collector surfaces. The analysis provided in the below figures will illustrate the differences in the deposition/dissolution microstructures between the Na₂Te@CF collector and the baseline CF.

Figure 2c,d compares the CEs of Na₂Te@CF, Na₂S@CF, and CF at 2 mA cm⁻² to 1 mAh cm⁻², and 4 mA cm⁻² to 2 mAh cm⁻², respectively. At both test conditions, the baseline CF shows unstable cycling with fluctuating CE from the onset. The Na₂S@CF electrode displays relatively stable CE in the first 100 cycles and then starts to become unstable. In comparison, Na₂Te@CF is stable for over 800 cycles with cumulative electrodeposition/electrodissolution capacities of 800 mAh cm⁻² at 2 mA cm⁻², and 1600 mAh cm⁻² at 4 mA cm⁻². Since 1 mAh cm⁻² of Na metal corresponds to a ≈9 μm film, a cycled capacity of 1600 mAh cm⁻² corresponds to 14.4 mm of metal (by geometrical area) that is ultimately electrodeposited/electrodissolved. Figure 2e compares the crystallite nucleation and subsequent film growth overpotentials during cycling, tested at 2 mA cm⁻² to 1 mAh cm⁻². The major difference among the three samples occurs during the nucleation stage, when Na crystallites are first formed on the exposed Na₂Te@CF, Na₂S@CF, and CF surfaces. The Na₂Te@CF sample exhibits the lowest nucleation overpotential with an average of 26 mV, in contrast to 31 mV for Na₂S@CF and 45 mV for baseline CF. The difference in the nucleation overpotentials between Na₂Te@CF and Na₂S@CF is likely a direct outcome of the difference in the energetics for Na atom adhesion, per the DFT results shown later in the manuscript. The film growth-related overpotentials are on-par, being on the order of 24 mV for all three specimens. This is reasonable since once a layer of Na crystallites fully covers the substrate surface, the interactions are between the “new” Na metal and the underlying Na metal.

Figure 2f provides cycle 151–156 galvanostatic profiles for Na₂Te@CF, Na₂S@CF, and CF, tested at 2 mA cm⁻² to 1 mAh cm⁻². The half-cell based on Na₂Te@CF shows a stable electrodeposition/electrodissolution profile, while both Na₂S@CF and CF exhibit deteriorating electrodischarge profiles with associated voltage instability. The deterioration associated with CF is substantially worse than with Na₂S@CF. Figure S15, Supporting Information, provides SEM and associated EDXS map of the Na₂Te@CF electrode in the electrodischarged condition. The sample underwent 50 cycles at 2 mA cm⁻² to 1 mAh cm⁻². From the SEM images and the EDXS map of Te, Na, and Cu, it may be concluded that the surface remains uniformly covered by the sodiophilic layer.

Figure S16a–c, Supporting Information, provides a comparison of the half-cell cycling performance Na₂Te@CF and CF at

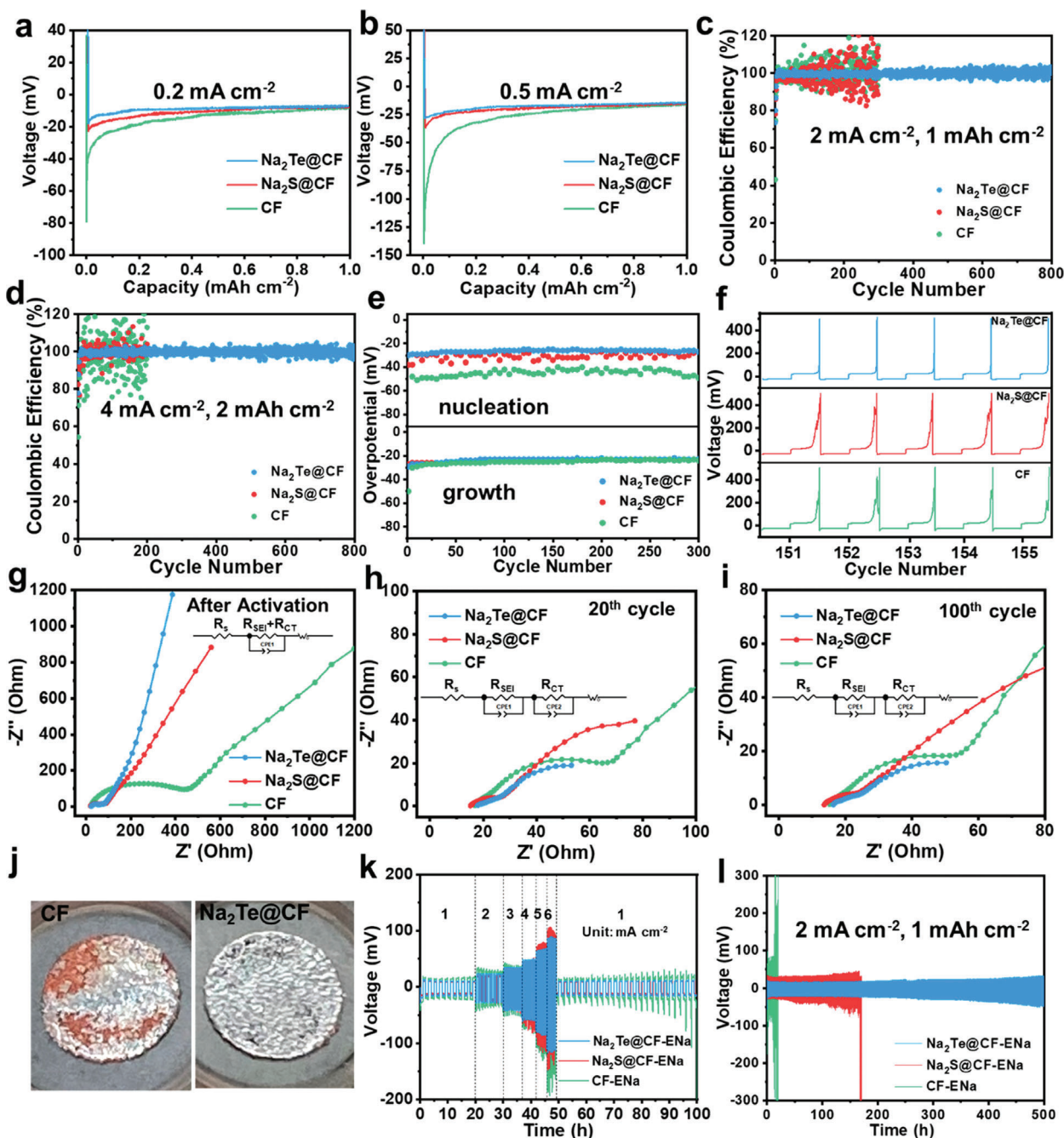


Figure 2. Electrochemical performance of the half cells and symmetrical cells based on the $\text{Na}_2\text{Te@CF}$, $\text{Na}_2\text{S@CF}$, and baseline CF. a,b) Galvanostatic profiles of electrodeposition at 0.2 and 0.5 mA cm^{-2} , respectively. c,d) Half-cell CE tests at c) 2 mA cm^{-2} to 1 mAh cm^{-2} capacity and d) 4 mA cm^{-2} to 2 mAh cm^{-2} capacity. e) Nucleation and growth overpotentials at 2 mA cm^{-2} to 1 mAh cm^{-2} capacity. f) Representative galvanostatic profiles of half-cells, taken at cycles 151 to 155 at 2 mA cm^{-2} to 1 mAh cm^{-2} capacity. g–i) Nyquist plots of the three substrates tested at 2 mA cm^{-2} to 1 mAh cm^{-2} capacity after different cycles with respective equivalent circuit shown as the inset. j) Digital photographs of the CF and $\text{Na}_2\text{Te@CF}$ surfaces after electrodepositing a capacity of 5 mAh cm^{-2} Na at 0.5 mA cm^{-2} . k) Rate capability with a fixed capacity of 1 mAh cm^{-2} at different current densities. l) Cycling performance at 2 mA cm^{-2} to 1 mAh cm^{-2} capacity.

extreme conditions: The electrodeposited/electrodissolved capacity is 5 mAh cm^{-2} while the current density is 5 mA cm^{-2} . The results highlight how significant of a difference does the current collector surface make. The working electrode based on $\text{Na}_2\text{Te@CF}$ is stable at 300 cycles, while baseline CF exhibits a

fluctuating profile from the onset. Figure S16d, Supporting Information, provides data for an even more aggressive cycling regimen, 6 mAh cm^{-2} at 6 mA cm^{-2} , corresponding to 54 mm of Na metal (by geometrical area) being electrodeposited or electrodis-solved per hour. Again the $\text{Na}_2\text{Te@CF}$ electrode is stable over 200

cycles. Figure S17, Supporting Information, shows additional cycling data, collected at 2 mA cm⁻² to 2, 5, and 10 mAh cm⁻², and at 6 mA cm⁻² to 3 mAh cm⁻². The half-cell based on Na₂Te@CF exhibits the most stable behavior in terms of overpotentials and CEs. Figure S18, Supporting Information, provides the half-cell cycling data with different Te loadings, collected at 2 mA cm⁻² to 1 mAh cm⁻², and 4 mA cm⁻² to 2 mAh cm⁻². The cells with a higher mass loading of Na₂Te display greater cycling stability, although all exhibits improved cycling compared to baseline CF. The higher loading leads to relatively more sodiophilic sites that are available for Na electrodeposition/electrodissolution. Table S2, Supporting Information, compares the asymmetric half-cell performance in terms of current density, electrodeposition capacity, and cycle life of Na₂Te@CF with state-of-the-art Na metal hosts in previous literature. It may be observed that the performance of Na₂Te@CF is among the most favorable.

Figure 2g-i provides the EIS Nyquist plots for Na₂Te@CF, Na₂S@CF, and CF half-cells, directly after the in situ activation but prior to any cycling, after 20 cycles, and after 100 cycles. The electrodes were tested at 2 mA cm⁻² to 1 mAh cm⁻² capacity. The inset in each figure shows the respective equivalent circuit used to fit the data, the impedance values being provided in Table S3, Supporting Information. Both Na₂Te@CF and Na₂S@CF exhibit significantly lower combined SEI and charge-transfer resistance ($R_{\text{SEI}} + R_{\text{CT}}$) than the baseline CF. After the in situ activation these values are 32, 40, and 475 Ω , respectively. This indicates that the substrate energetics have a direct influence on the resistance associated with the complex interphase interface of the metal and the electrolyte. The conclusion is somewhat non-intuitive but will be elaborated further later in the manuscript through characterization and modeling. The difference in the interfacial resistance among the three specimens is further amplified after 20 and 100 cycles, where the two resistances R_{SEI} and R_{CT} can be effectively distinguished. The SEI resistance with Na₂Te@CF is the lowest at 8 Ω , which is indicative of a thinner and less resistive SEI. The Na₂Te@CF also maintains the lowest R_{CT} after 20 and 100 cycles, remaining stable at 49 and 58 Ω . For Na₂S@CF the R_{CT} increases from 144 to 245 Ω , while for baseline CF it increases from 210 to 292 Ω .

Figure 2j and Figure S19, Supporting Information, show digital photographs of the Na₂Te@CF, Na₂S@CF, and CF current collectors, disassembled after electrodepositing 5 mAh cm⁻² Na at 0.5 mA cm⁻². The photographs highlight the macroscopic uniformity of the electrodeposited metal on Na₂Te@CF and Na₂S@CF but not on the baseline CF. This finding that the deposited Na film on a sodiophilic surface is irregular from the start, indicates that dendritic growth is effectively “baked in.” It is the normal state for an unmodified Cu support, rather than some anomalous process that evolves with cycling beyond a critical current.

To evaluate symmetric cell performance, a capacity of 5 mAh cm⁻² Na was first pre-electrodeposited onto a working electrode in a half-cell configuration. Two such half-cells were then disassembled, with their working electrodes being then reassembled into a symmetric cell filled with fresh electrolyte. Figure 2k,l contrasts the rate capability and cycling stability of these cells. As shown in the figures, the baseline CF cell displays much larger overpotentials than either of the coated specimens. The rate capability difference between Na₂S@CF and Na₂Te@CF is not ob-

vious until the current is raised to 4 mA cm⁻², at which point the Na₂S@CF specimen becomes less stable with larger overpotentials. The cycling performance shows the same trend with the Na₂Te@CF symmetric cell having the lowest overpotential and being the most stable. The CF and Na₂S@CF cells fail earlier, with significant voltage fluctuations occurring by cycles 21 and 167, respectively. By contrast, the Na₂Te@CF cell remains stable at 500 cycles.

The role of metal-support energetics electrochemical properties of symmetric cells requires further examination. With both CF and Na₂Te@CF the metal electrodeposits/electrodissolves onto/from pre-existing sodium reservoirs. The composite support layer clearly makes a significant difference, however. We hypothesize that there is a preferred nucleation crystallography or even epitaxy associated with depositing Na crystallites onto pre-existing Na film surfaces. The microstructure of the Na metal with Na₂Te@CF is more favorable for low energy nucleation than that of the metal deposited on the baseline CF. This may be related to the differences in the grain sizes and grain crystallographic textures between the two metal films. The major difference in the SEI morphology should also influence the electrodeposition/electrodissolution overpotentials, as would the resulting stress state of the support. Increased electrodeposition overpotential has been linked to promoting island-like rather than planar film growth.^[95,96] Therefore differences in the SEI that lead to differences in the overpotentials could in-turn lead to differences in the wetting behavior of Na metal on Na metal. For example, the thicker and less regular SEI layer with baseline CF could lead to Stranski–Krastanov type of dewetting of the “new” electrodeposit from the “old” underlying metal film.

Figure 3 and Figures S20 and S21, Supporting Information, present top-down SEM images and associated EDXS maps comparing Na₂Te@CF versus baseline CF at various electrodeposited/electrodissolved conditions, tested at 1 mA cm⁻². Figure 3a–h displays the analysis of Na₂Te@CF at increasing Na electrodeposition capacity, starting with 1 mAh cm⁻² and concluding with 5 mAh cm⁻². The top and bottom rows show the low and high magnification images, respectively. Figure 3i–p presents the analysis of CF under the same conditions. It may be observed that with increasing capacity the sodium electrodeposit forms uniformly on the surface of the Na₂Te@CF, being dense, flat, and with no evidence of dendrites. For baseline CF, the width of the filament-like dendrites appears to be relatively invariant with the deposited capacity. This would be expected if the filaments nucleated with certain stable dimensions and lengthened with increasing amount of electrodeposited metal. However there is also a lot of region-to-region variation in the scale of the filaments, explaining why the filaments appear longer at 3 mAh cm⁻² than at 5 mAh cm⁻². In summary, on bare CF surface, sodium metal naturally grows in a filament-like manner and does not require cycling to achieve this highly deleterious geometry.

Figure 4 provides cross-sectional cryo-FIB-SEM analysis and EDXS maps of Na electrodeposition and remnant electrodis-solved microstructures of Na₂Te@CF and baseline CF. Sample preparation and analysis details for cryo-EM are provided in the Supporting Information. For Figure 4a–h, sodium metal was analyzed at electrodeposited capacities ranging from 0.5 to 5 mAh cm⁻². For Figure 4i–l, analysis was performed after electrodepositing 5 mAh cm⁻² followed by electrodis-solution to 1 V.

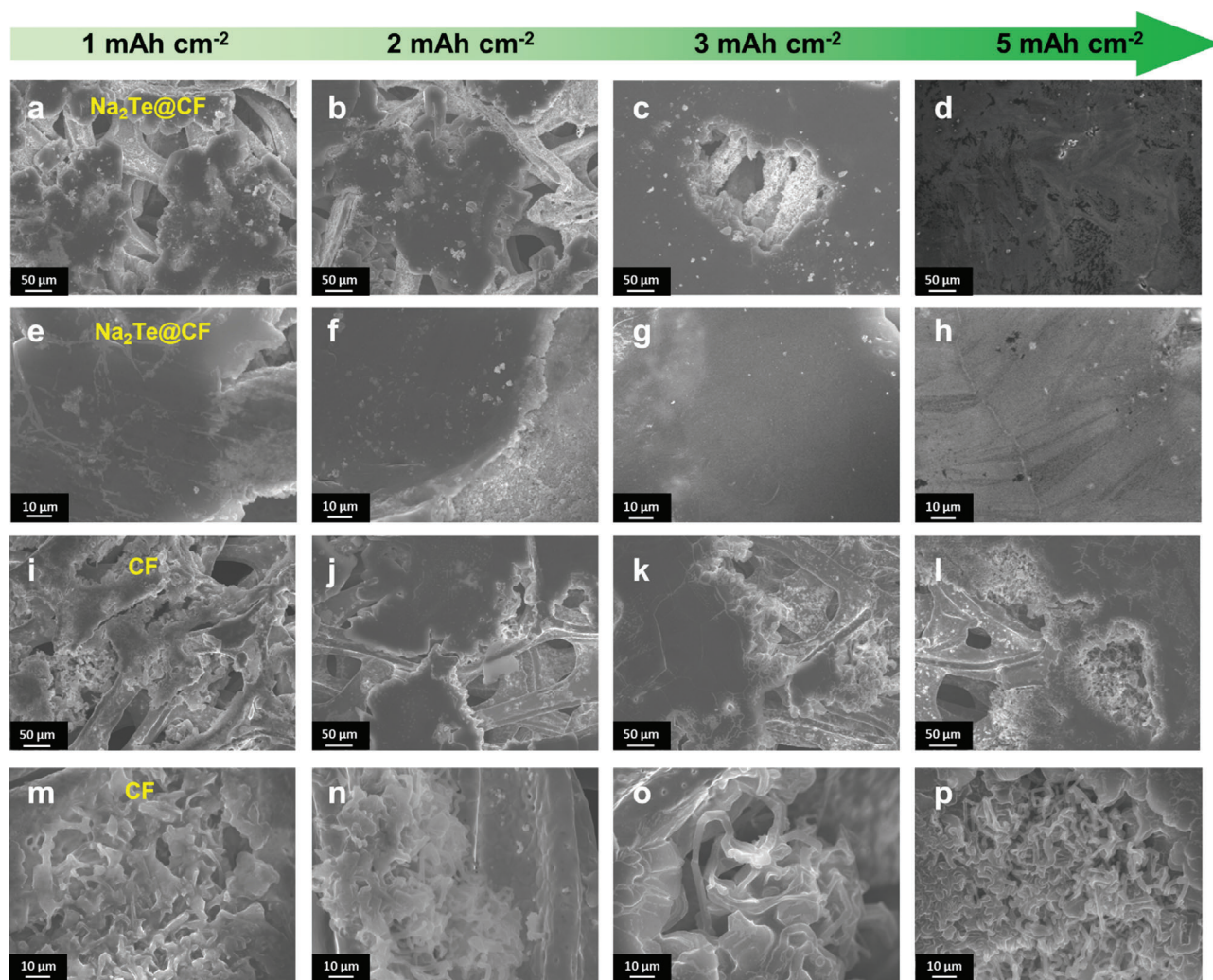


Figure 3. a–d) low magnification and e–h) high magnification SEM images of $\text{Na}_2\text{Te}@CF$ with different Na electrodeposition capacities. i–p) Same analysis for baseline CF. A current density of 1 mA cm^{-2} was employed.

An electrodeposited capacity of 0.5 mAh cm^{-2} corresponds to 4.5 mm thickness of a fully dense deposit by geometrical area, while 5 mAh cm^{-2} corresponds to 45 mm . The observed structures are consistent with the top-down SEM results. The sodium metal electrodeposited onto $\text{Na}_2\text{Te}@CF$ is dense, smooth, and pore-free. The electrodeposit on baseline CF is in effect a triphasic sponge of sodium metal filaments interspersed with a thick SEI and with pores. As expected, this porous SEI remains in the terminally electrodissoved state. At the same electrodissoved condition, the surface of the $\text{Na}_2\text{Te}@CF$ remains covered by the Na_2Te and Cu particles, with the SEI layer being markedly thinner. Per the EDXS maps the Cu is interspersed with the Na_2Te . These findings demonstrate a direct relationship between the metal–current collector interfacial chemistry and the metal–electrolyte interphase structure. The presence Na_2Te directly influences the SEI thickness, distribution, and morphology both in the electrodeposited and electrodissoved states.

The enhanced early-stage wetting behavior of Na on the $\text{Te}@CF$ surface was further investigated by DFT and mesoscale simulations. The approach is based on comparing the binding

energy between Na single atoms to Na clusters with 4–5 atoms. Details of the methodology have been outlined.^[97] During the early-stage electrodeposition of sodium on anode surfaces, if it is thermodynamically more stable to form clusters than atomic dispersion, then this wetting behavior will promote the growth of 3D islands instead of planar thin films. On the other hand, if atomic dispersion is preferred thermodynamically, a uniform electrodeposited film will be formed consequently with minimal island/dendritic growth. It is noteworthy that in all calculations, each type of substrate remains consistent despite some variations in atomic arrangements, due to the fact that during optimization with adatoms, the position of surface atoms also undergoes optimization, influenced by interatomic interactions of adatoms on the surface. All figures display unit cells used for the calculation and the arrangement is periodic in the plane. For example, Figure 5a–d represents the same Na_2Te (110) surfaces, with the only variation being the position of one Te atom at the bottom in Figure 5b compared to Figure 5a,c,d. This difference is a result of the optimization process where Te atom optimizes to a slightly different position on the surface.

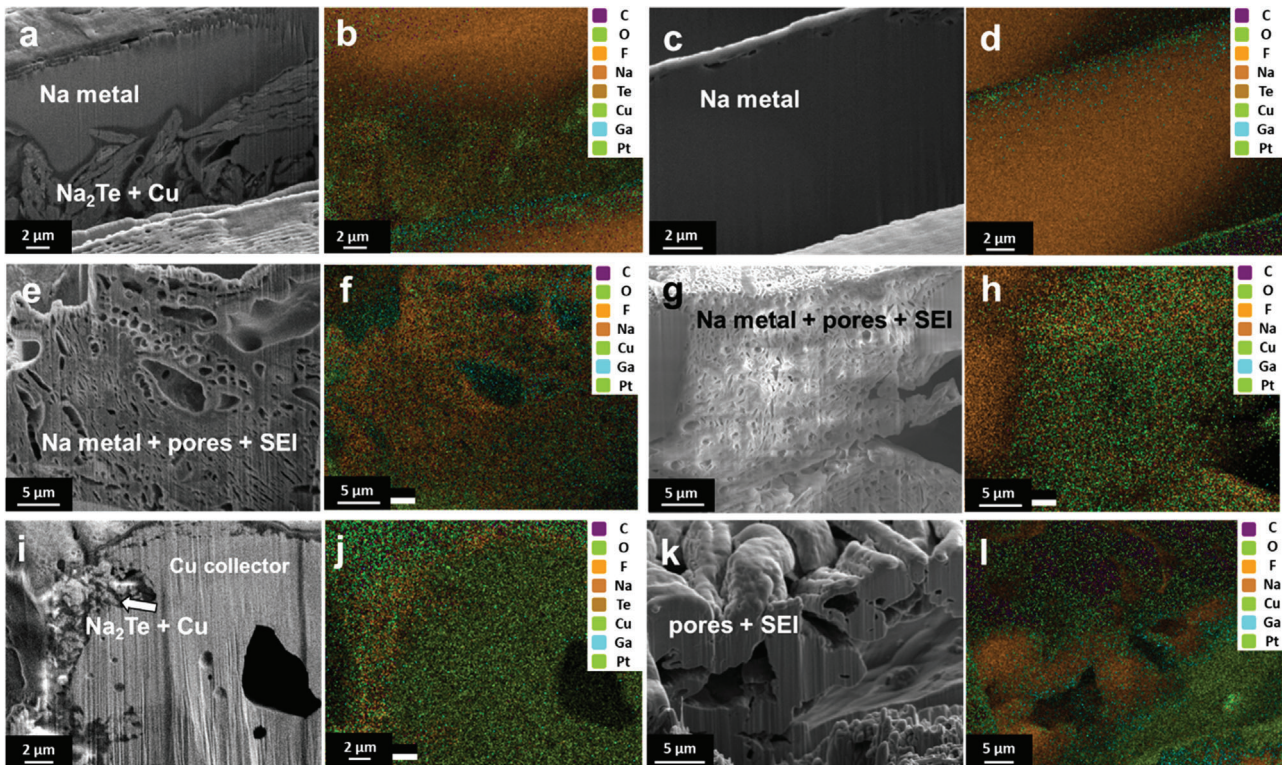


Figure 4. Cross-sectional cryo-FIB-SEM analysis of Na electrodeposition/electrodissolution on Na₂Te@CF and baseline CF, tested at 1 mA cm⁻². a,b) Na₂Te@CF with a capacity of 0.5 mAh cm⁻². c,d) Na₂Te@CF with a capacity of 5 mAh cm⁻². e–h) Same analysis for baseline CF. Analysis of i,j) Na₂Te@CF and k,l) CF after electrodepositing 5 mAh cm⁻² Na followed by electrodisolution to 1 V.

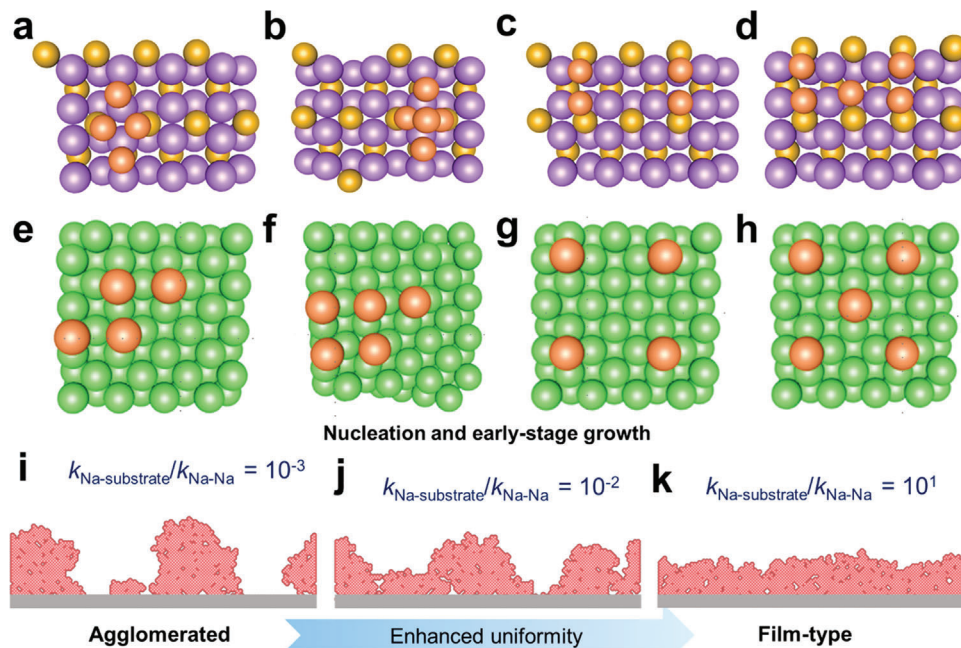


Figure 5. Multiscale simulation of the interactions of Na with Na₂Te and Cu surfaces: a–h) DFT simulation. i–k) Kinetic Monte Carlo simulation. a,b) Na₄ cluster and Na₅ cluster on fcc Na₂Te surface, c,d) four and five individual Na atoms on fcc Na₂Te surface. e,f) Na₄ cluster and Na₅ cluster on fcc Cu surface, g,h) four and five individual Na atoms on fcc Cu surface. Color scheme: Na (purple), Te (yellow), Cu (green), and Na in the binding site (orange). i–k) Nucleation and early-stage growth morphology as a function of the Na-substrate interaction.

Table 1. Binding energies for four or five sodium atoms and sodium clusters on the relevant surfaces.

Binding Energy per Na [eV]	Four Na atoms	Na ₄ cluster	Five Na atoms	Na ₅ cluster
(110) fcc Na ₂ Te	0.17	0.23	0.19	0.27
(110) fcc Na ₂ S	0.05	0.31	0.22	0.23
(111) fcc Cu	-1.21	-1.21	-0.67	-0.69
(110) bcc Na	0.19	0.10	0.16	0.06
(111) fcc NaF	-0.55	-0.59	-0.47	-0.68
(111) fcc Na ₂ O	-0.66	-0.95	-0.77	-0.94

Representative structures of Na₄/Na₅ clusters and atomically dispersed Na₄/Na₅ on different modeled surfaces are shown in Figure 5a–h and Figure S22, Supporting Information. The calculated binding energies (with respect to sodium atoms in bulk) are shown in Table 1. The most positive binding energy corresponds to the least thermodynamically stable configuration. For the Na₂Te surface, the sodium atomic dispersion is thermodynamically more stable than sodium clusters because tellurium atoms on the surface prefer to bind with sodium in an arrangement similar to layers underneath during the early stages of electrodeposition, leading to complete coverage of the support surface and thin film formation. This is different for the Cu (111) surface, where there is no thermodynamic preference between sodium clusters and atomic dispersion due to the absence of any preferred sodium deposition morphology. This suggests that experimentally observed early-stage electrodeposited film morphology is governed by kinetic factors like the Na ion flux heterogeneity through the liquid electrolyte and solid SEI. With Na₂S, four Na atoms are significantly more stable than clusters, but there is negligible difference between five atoms and clusters, which demonstrates the difference between Te and S but is still better than Cu. The results confirm that the sodiophilic substrates would enable a uniform Na deposition.

It is also important to appreciate that residue SEI can aggravate the dendrite growth if electrodeposition occurs on its surface due to mixed ion–electron conduction, rather than underneath it. Calculations were performed on the (111) surface of NaF and Na₂O and the results show that both surfaces favor the growth of Na clusters rather than atoms. This suggests that the residue SEI can aggravate the dendrite growth, which is intriguing as NaF and Na₂O are commonly found as inorganic SEI components that suppress electrode corrosion and prevent dendrite growth, with recent studies showing the enriching the SEI with NaF can improve Na cycling stability.^[55,98–101] However, as substrates for Na deposition, NaF and Na₂O are less favorable. Although no reports have examined the role of NaF and Na₂O as substrates, similar studies have been conducted on Li electrodeposition on LiF-containing substrates. For example, Xie et al.^[102] prepared LiF coated Cu using atomic layer deposition (ALD) method and observed that the electrodeposition of Li on LiF/Cu was worse than on bare Cu, with dendritic Li deposits in both cases. Gallant et al.^[103] treated pristine Li with nitrogen trifluoride gas to form a compact LiF layer on the surface. The LiF-coated Li exhibited a high interfacial resistance, leading to increased overpotentials during Li electrodeposition/electrodissolution. Moreover, the LiF

layer did not prevent the Li dendrite formation and gradually degraded during cycling. Since LiF and NaF share similar properties, comparable effects are predicted for NaF as a substrate for Na deposition. Therefore, our binding energy calculations of Na on NaF and Na₂O substrates are consistent with experimental observations that fluoride and oxide products cannot impede the dendritic growth when the metal is electrodeposited on top of these substrates.

To elucidate the enhancement of Na wettability on Na₂Te@CF as compared to Na₂S@CF, the work of adhesion of Na–Na₂Te and Na–Na₂S was calculated, and a detailed calculation approach is shown in the Supporting Information. The adhesion energy between Na and Na₂Te is 0.41 J m⁻², whereas the adhesion energy between Na and Na₂S is 0.27 J m⁻². A stronger work of adhesion is associated with the stronger binding, therefore Na wets Na₂Te better than Na₂S, which helps explain the improved performance of Na₂Te@CF over Na₂S@CF in terms of nucleation behavior during electrodeposition, as well as subsequent cycling stability which is degraded by island growth and the associated inhomogeneous SEI.

To mechanistically understand the evolution of the electrodeposition morphologies beyond the atomic scale, we developed a mesoscale model based on the kinetic Monte Carlo algorithm. Such models have been shown effective in connecting the substrate–metal interactions to the nucleation and early-stage growth behavior.^[104–106] The nucleation response is dependent on the binding behavior of Na on the substrate and the binding behavior of Na on the newly formed Na deposits. The competing nature of this adsorption mechanism at the substrate–metal interface during the nucleation phase is described using $k_{\text{Na-substrate}}/k_{\text{Na-Na}}$, as illustrated in Figure 5i–k. Here, $k_{\text{Na-substrate}}$ denotes the adsorption kinetics of Na on the substrate and $k_{\text{Na-Na}}$ denotes the adsorption kinetics of Na on the freshly electrodeposited Na metal. The details about the simulation approach to capture the dynamic growth of the deposition morphologies are presented in the Supporting Information. As shown in Figure 5i, a weaker metal–substrate interaction (i.e., corresponding to a lower $k_{\text{Na-substrate}}/k_{\text{Na-Na}}$) leads to the preferential adsorption of Na on the freshly formed Na nuclei when compared to the substrate surface. This regime involves the formation of isolated Na deposits and limited nuclei coverage over the substrate, per Figure 5i. This in turn results in a non-homogeneous reaction distribution for the subsequent growth phase. With an increase in $k_{\text{Na-substrate}}/k_{\text{Na-Na}}$, a transition in the nucleation morphology from an agglomerated pattern to a film-like deposit occurs, along with a substantial improvement in the substrate coverage. These results are shown in Figure 5i–k. According to Figure 5k, driven by the preferential metal coverage on the substrate, the formation of a film-like nucleation morphology is critical toward achieving uniform flux distribution and preventing the onset of potential reaction hotspots. The DFT calculations and the mesoscale model provide consistent insights at different scales into the relationship between the substrate–metal interaction and the nucleation response.

As proof-of-principle full cell SMBs were fabricated and tested. The cells employed Na₃V₂(PO₄)₃ (NVP) cathodes combined with thermally infused “T” Na anodes and thick Na foil. Thermal infusion of Na provides a rapid and potentially industry-scalable route to fabricate metal anodes. For demonstration, Te@CF and

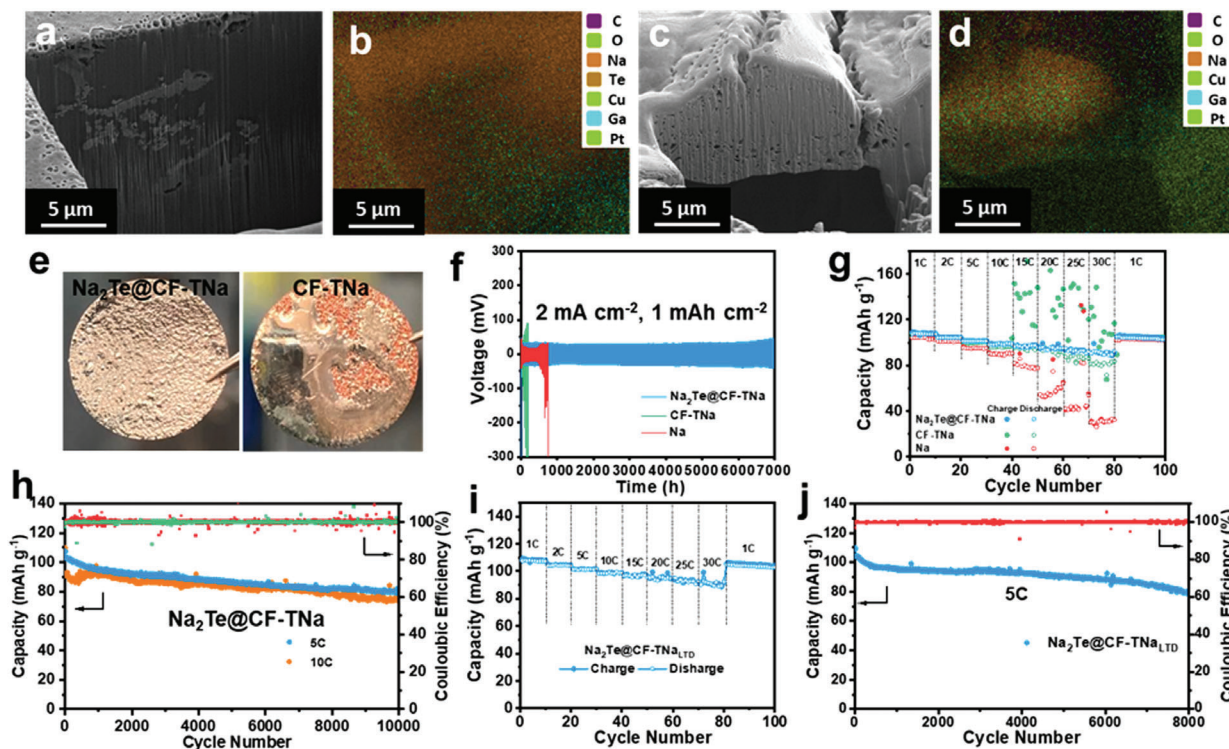


Figure 6. Cryo-FIB-SEM image with EDXS maps of a,b) $\text{Na}_2\text{Te}@CF\text{-TNa}$ and c,d) $CF\text{-TNa}$. e) Digital photos showing the $\text{Na}_2\text{Te}@CF\text{-TNa}$ and $CF\text{-TNa}$ electrodes. f) Cycling performance of symmetric cells at 2 mA cm^{-2} to 1 mA h cm^{-2} . g) Rate capability of full cells with $\text{Na}_2\text{Te}@CF\text{-TNa}$, $CF\text{-TNa}$, and Na anodes and NVP cathodes ($1\text{C} = 118\text{ mA g}^{-1}$). h) Cycling performance of $\text{Na}_2\text{Te}@CF\text{-TNa}||\text{NVP}$ full cells. i) Rate capability and j) Cycling performance of $\text{Na}_2\text{Te}@CF\text{-TNa}_{\text{LTD}}||\text{NVP}$ full cells.

CF were immersed in molten Na and the resulted composite electrodes are denoted as $\text{Na}_2\text{Te}@CF\text{-TNa}$ and $CF\text{-TNa}$, respectively. **Figure 6a–e** provides cross-sectional cryo-FIB-SEM and associated EDXS analysis and light optical photographs of these two specimens after thermal Na infusion. **Figure S23**, Supporting Information, shows the surface SEM images of $\text{Na}_2\text{Te}@CF\text{-TNa}$ where smooth and uniform Na metal coverage can be observed after the thermal impregnation. The thermally infused Na on baseline CF is macroscopically non-uniform, with large sections of the Cu foam being exposed due to poor wetting of the molten metal. By contrast, Na is uniformly impregnated onto the sodiophilic $\text{Na}_2\text{Te}@CF$, being uniform and relatively free from porosity. Some of the Na_2Te particles appear to have been dislodged from the Cu substrates and appear closer to the bulk of the Na film. To compare the wettability of molten Na on different substrates, a Na wetting experiment was conducted by placing a small Na chunk on top of the preheated $\text{Te}@CF$ or CF substrates. As demonstrated in **Figure S24**, Supporting Information, the Na wetting behavior of $\text{Te}@CF$ has been significantly improved, as the melted Na was uniformly and completely infused into $\text{Te}@CF$ and the contact angle was reduced to almost 0° . By contrast, the melted Na did not wet the baseline CF substrate. The contact angle of melted Na on CF was measured to be 138° , confirming its non-wetting behavior. **Movies S1 and S2**, Supporting Information, provide a comprehensive demonstration of the Na wetting experiment process.

Figure 6f and **Figures S25–S27**, Supporting Information, show the electrochemical performance of $\text{Na}_2\text{Te}@CF\text{-TNa}$, baseline

$CF\text{-TNa}$, and baseline Na in half-cell (symmetric cells) configurations. **Figure S25**, Supporting Information, provides the rate capability of these three specimens, tested under various current densities to reach a targeted capacity of 2 mA h cm^{-2} . It may be observed that the $\text{Na}_2\text{Te}@CF\text{-TNa}$ electrode shows much lower voltage polarization under each current density and the difference versus the baseline increases with current. **Figure 6f** shows the voltage versus time profiles, tested at 2 mA cm^{-2} to 1 mA h cm^{-2} . The baseline $CF\text{-TNa}||CF\text{-TNa}$ and $\text{Na}||\text{Na}$ cells display early onsets of unstable voltages, with marked deteriorations starting from cycles 138 and 658, respectively. By contrast, the $\text{Na}_2\text{Te}@CF\text{-TNa}||\text{Na}_2\text{Te}@CF\text{-TNa}$ cells remain stable even after 7000 h with a cumulative capacity of 7000 mA h cm^{-2} , which is among the most favorable per **Table S4**, Supporting Information. **Figure S26**, Supporting Information, shows additional cycling data of $\text{Na}_2\text{Te}@CF\text{-TNa}$, collected at 1 mA cm^{-2} to 2 mA h cm^{-2} , 2 mA cm^{-2} to 3 mA h cm^{-2} , 2 mA cm^{-2} to 4 mA h cm^{-2} , 2 mA cm^{-2} to 10 mA h cm^{-2} , and 5 mA cm^{-2} to 5 mA h cm^{-2} . Here again, $\text{Na}_2\text{Te}@CF\text{-TNa}$ cells display excellent stability at each testing condition. In addition, it has been known that it is challenging to achieve a stable cycling of Na metal anode in carbonate electrolytes due to its high corrosivity toward Na metal.^[107,108] **Figure S27**, Supporting Information, provides the cycling performance of $\text{Na}_2\text{Te}@CF\text{-TNa}$ and $CF\text{-TNa}$ in carbonate electrolytes composed of 1 M NaClO_4 in $\text{EC}:\text{PC}$ (1:1 by volume) with $10\text{ wt}\%$ FEC , tested at 0.5 mA cm^{-2} to 1 mA h cm^{-2} and 1 mA cm^{-2} to 1 mA h cm^{-2} . In both cases, the galvanostatic profile of baseline $CF\text{-TNa}$ deteriorates at a much early stage, starting from cycles 22 and

9, respective. By contrast, the $\text{Na}_2\text{Te}@CF\text{-TNa}$ maintains stable cycling up to 800 and 350 h.

To further evaluate the feasibility of $\text{Na}_2\text{Te}@CF\text{-TNa}$ anodes in SMBs, full cells were assembled based on NVP cathodes combined with $\text{Na}_2\text{Te}@CF\text{-TNa}$ or CF-TNa or Na. Figure 6g shows the rate capability of $\text{Na}_2\text{Te}@CF\text{-TNa}||\text{NVP}$, CF-TNa||NVP, and Na||NVP cells with currents gradually increasing from 1C, 2C, 5C, 10C, 15C, 20C, 25C to 30C. The $\text{Na}_2\text{Te}@CF\text{-TNa}||\text{NVP}$ cell exhibits reversible capacities of 108, 104, 101, 99, 97, 95, 93, and 91 mAh g^{-1} , respectively. After switching the current from 30C back to 1C, a specific capacity of 105 mAh g^{-1} can be recovered. By contrast, the baseline CF-TNa||NVP and Na||NVP exhibit lower capacities under every current and overcharge when the current exceeds 15C. The charge process in the full cell corresponds to the Na electrodeposition on the substrates and therefore the severe overcharge in CF-TNa||NVP cell can be ascribed to the unfavorable Na deposition on the sodiophobic surface of CF-Na. Figure S28, Supporting Information, provides the galvanostatic charge/discharge profiles under each current density. It can be concluded that the $\text{Na}_2\text{Te}@CF\text{-TNa}||\text{NVP}$ cell delivers a much smaller polarization voltage, especially under high current densities, implying that the sodiophilic layer can effectively enhance the diffusion kinetics and enable fast charging/discharging of SMBs. Figure 6h displays the long cycling performance of $\text{Na}_2\text{Te}@CF\text{-TNa}||\text{NVP}$ cells. Impressively, reversible capacities of 80 and 75 mAh g^{-1} can be obtained after 10 000 cycles at high currents of 5C and 10C, respectively. Such electrochemical performance is among the most favorable, per Table S5, Supporting Information.

To achieve a limited Na infusion, a small piece of Na metal was first weighed (≈ 4 mg) and melted on the hot plate. The Te@CF was then placed on the top of the molten Na droplet and due to the strong sodiophilic surface, molten Na can be easily impregnated into its skeleton and the obtained composite is denoted as $\text{Na}_2\text{Te}@CF\text{-TNa}_{\text{LTD}}$ where “LTD” subscript stands for “Limited.” Figure S29, Supporting Information, shows the voltage versus capacity profile of Na after attempting to electrodisolve the Te@CF-TNa_{LTD} to a cutoff voltage of 0.5 V. Approximately 4.6 mAh Na was extracted from the electrode, corresponding to an areal Na loading of 5.8 mAh cm^{-2} and a total amount of ≈ 3.9 mg Na, which indicates that almost all initially added Na was impregnated into the Te@CF and remains active during the subsequent electrodisolution process. To demonstrate the electrochemical performance of $\text{Na}_2\text{Te}@CF\text{-TNa}_{\text{LTD}}$ electrodes, full cells coupled with NVP cathodes were assembled. Figure 6i displays the rate performance of the $\text{Na}_2\text{Te}@CF\text{-TNa}_{\text{LTD}}||\text{NVP}$ cell, which delivers almost the same capacities under each current as the $\text{Na}_2\text{Te}@CF\text{-TNa}||\text{NVP}$ cell. In addition, the $\text{Na}_2\text{Te}@CF\text{-TNa}_{\text{LTD}}||\text{NVP}$ still has a specific capacity of 80 mAh g^{-1} over 8000 cycles at 5C with a CE of $\approx 100\%$. Those results are shown in Figure 6j.

3. Conclusions

In this study, sodiophilic current collectors based on sodium chalcogenide intermetallic coated commercial copper foam ($\text{Na}_2\text{Te}@CF$ and $\text{Na}_2\text{S}@CF$) are fabricated through a combination of rapid thermal evaporation and kinetically irreversible in situ electrochemical reaction. These substrates result in significantly reduced electrodeposition/electrodisolution overpoten-

tials and improved Coulombic efficiency (CE). A controllable capacity Na thermal infusion process is also demonstrated. State-of-the-art electrochemical performance is achieved in half-cell, symmetric cell, and full battery cell architectures based on NVP cathodes. Cryogenic focused ion beam (cryo-FIB) analysis shows early-stage electrodeposition behavior being important for later-stage cycling. Sodium metal electrodeposits uniformly on $\text{Na}_2\text{Te}@CF$ resulting in dense and pore-free metal without evidence of dendrites even at ≈ 45 nm deposited film thickness (5 mAh cm^{-2}). Electrodeposits on baseline uncoated CF are filament-like dendrites interspersed with pores and SEI. In the terminally electrodisolved condition, extensive porous SEI covers the CF surface. DFT and mesoscale simulations provide combined insight into the relationship between substrate–metal interaction and the nucleation response, describing the underlying mechanisms that dictate the film microstructure.

Supporting Information

Supporting Information is available from the Wiley Online Library or from the author.

Acknowledgements

This work was supported by the U.S. Department of Energy, Office of Basic Energy Sciences, Division of Materials Sciences and Engineering under Award # DE-SC0023260. Cryo-EM was performed at the Center for Integrated Nanotechnologies, an Office of Science User Facility operated for the U.S. Department of Energy (DOE) Office of Science. The Los Alamos National Laboratory, an affirmative action equal opportunity employer, is managed by Triad National Security, LLC for the U.S. Department of Energy's NNSA, under contract 89233218CNA000001. DFT calculations by N.K. and G.H. were supported by the Welch Foundation (F-1841), and computing resources at the Extreme Science and Engineering Discovery Environment (XSEDE)/Advanced Cyberinfrastructure Coordination Ecosystem: Services and Support (ACCESS) and the Texas Advanced Computing Center (TACC) with the allocation CHE190010—Modeling Materials for Energy Conversion and Storage over Experimental Timescales.

Conflict of Interest

The authors declare no conflict of interest.

Data Availability Statement

The data that support the findings of this study are available from the corresponding author upon reasonable request.

Keywords

anode-free batteries, cryogenic electron microscopy, metal dendrites, sodium ion batteries

Received: December 28, 2022
Revised: March 18, 2023
Published online: April 25, 2023

[1] R. Schmuck, R. Wagner, G. Hörpel, T. Placke, M. Winter, *Nat. Energy* **2018**, *3*, 267.

- [2] E. M. Erickson, C. Ghanty, D. Aurbach, *J. Phys. Chem. Lett.* **2014**, *5*, 3313.
- [3] L. Mai, M. Yan, Y. Zhao, *Nat. Energy* **2017**, *546*, 469.
- [4] N. Yabuuchi, K. Kubota, M. Dahbi, S. Komaba, *Chem. Rev.* **2014**, *114*, 11636.
- [5] H. Pan, Y.-S. Hu, L. Chen, *Energy Environ. Sci.* **2013**, *6*, 2338.
- [6] W. Luo, F. Shen, C. Bommier, H. Zhu, X. Ji, L. Hu, *Acc. Chem. Res.* **2016**, *49*, 231.
- [7] D. Bin, F. Wang, A. G. Tamirat, L. Suo, Y. Wang, C. Wang, Y. Xia, *Adv. Energy Mater.* **2018**, *8*, 1703008.
- [8] D. Gong, C. Wei, Z. Liang, Y. Tang, *Small Sci.* **2021**, *1*, 2100014.
- [9] L. Li, Y. Zheng, S. Zhang, J. Yang, Z. Shao, Z. Guo, *Energy Environ. Sci.* **2018**, *11*, 2310.
- [10] C. Bommier, D. Mitlin, X. Ji, *Prog. Mater. Sci.* **2018**, *97*, 170.
- [11] Y. Xie, E. Gabriel, L. Fan, I. Hwang, X. Li, H. Zhu, Y. Ren, C. Sun, J. Pipkin, M. Dustin, M. Li, Z. Chen, E. Lee, H. Xiong, *Chem. Mater.* **2021**, *33*, 4445.
- [12] K. Mongird, V. Viswanathan, P. Balducci, J. Alam, V. Fotedar, V. Koritarov, B. Hadjerioua, *Energies* **2020**, *13*, 3307.
- [13] K. Mongird, V. V. Viswanathan, P. J. Balducci, M. J. E. Alam, V. Fotedar, V. S. Koritarov, B. Hadjerioua, *Energy Storage Technology and Cost Characterization Report*, Pacific Northwest National Lab. (PNNL), Richland, WA, USA, **2019**.
- [14] X. Zhang, F. Hao, Y. Cao, Y. Xie, S. Yuan, X. Dong, Y. Xia, *Adv. Funct. Mater.* **2021**, *31*, 2009778.
- [15] W. Yin, G. Barim, X. Peng, E. A. Kedzie, M. C. Scott, B. D. McCloskey, M. M. Doeff, *J. Mater. Chem. A* **2022**, *10*, 25178.
- [16] M. D. Slater, D. Kim, E. Lee, M. Doeff, C. S. Johnson, *Adv. Funct. Mater.* **2013**, *23*, 947.
- [17] L. Wang, J. Shang, Q. Huang, H. Hu, Y. Zhang, C. Xie, Y. Luo, Y. Gao, H. Wang, Z. Zheng, *Adv. Mater.* **2021**, *33*, 2102802.
- [18] E. Goikolea, V. Palomares, S. Wang, I. R. Larramendi, X. Guo, G. Wang, T. Rojo, *Adv. Energy Mater.* **2020**, *10*, 2002055.
- [19] F. Wang, H. Yang, J. Zhang, P. Zhang, G. Wang, X. Zhuang, G. Cuniberti, X. Feng, *Adv. Mater.* **2018**, *30*, 1800028.
- [20] R. S. Longchamps, X.-G. Yang, S. Ge, T. Liu, C.-Y. Wang, *J. Power Sources* **2021**, *510*, 230416.
- [21] X. Chi, Y. Zhang, F. Hao, S. Kmiec, H. Dong, R. Xu, K. Zhao, Q. Ai, T. Terlier, L. Wang, L. Zhao, L. Guo, J. Lou, H. L. Xin, S. W. Martin, Y. Yao, *Nat. Commun.* **2022**, *13*, 2854.
- [22] P. K. Nayak, L. Yang, W. Brehm, P. Adelhelm, *Angew. Chem., Int. Ed.* **2018**, *57*, 102.
- [23] C. Delmas, *Adv. Energy Mater.* **2018**, *8*, 1703137.
- [24] J. Y. Hwang, S. T. Myung, Y. K. Sun, *Chem. Soc. Rev.* **2017**, *46*, 3529.
- [25] Y. Fang, X.-Y. Yu, X. W. Lou, *Matter* **2019**, *1*, 90.
- [26] Y. Sun, S. Guo, H. Zhou, *Adv. Energy Mater.* **2018**, *9*, 1800212.
- [27] B. Sun, P. Xiong, U. Maitra, D. Langsdorf, K. Yan, C. Wang, J. Janek, D. Schroder, G. Wang, *Adv. Mater.* **2020**, *32*, 1903891.
- [28] H. Yang, F. He, M. Li, F. Huang, Z. Chen, P. Shi, F. Liu, Y. Jiang, L. He, M. Gu, Y. Yu, *Adv. Mater.* **2021**, *33*, 2106353.
- [29] S. Guo, J. Yi, Y. Sun, H. Zhou, *Energy Environ. Sci.* **2016**, *9*, 2978.
- [30] W. Luo, L. Hu, *ACS Cent. Sci.* **2015**, *1*, 420.
- [31] J. Xiao, N. Xiao, K. Li, L. Zhang, X. Ma, Y. Li, C. Leng, J. Qiu, *Adv. Funct. Mater.* **2022**, *32*, 2111133.
- [32] X. Zhou, F. Liu, Y. Wang, Y. Yao, Y. Shao, X. Rui, F. Wu, Y. Yu, *Adv. Energy Mater.* **2022**, *12*, 2202323.
- [33] G. G. Eshetu, G. A. Elia, M. Armand, M. Forsyth, S. Komaba, T. Rojo, S. Passerini, *Adv. Energy Mater.* **2020**, *10*, 2000093.
- [34] C. Bao, B. Wang, P. Liu, H. Wu, Y. Zhou, D. Wang, H. Liu, S. Dou, *Adv. Funct. Mater.* **2020**, *30*, 2004891.
- [35] C. Chu, R. Li, F. Cai, Z. Bai, Y. Wang, X. Xu, N. Wang, J. Yang, S. Dou, *Energy Environ. Sci.* **2021**, *14*, 4318.
- [36] B. Lee, E. Paek, D. Mitlin, S. W. Lee, *Chem. Rev.* **2019**, *119*, 5416.
- [37] C. Wang, A. C. Thenuwara, J. Luo, P. P. Shetty, M. T. McDowell, H. Zhu, S. Posada-Perez, H. Xiong, G. Hautier, W. Li, *Nat. Commun.* **2022**, *13*, 4934.
- [38] Y. Zhao, K. R. Adair, X. Sun, *Energy Environ. Sci.* **2018**, *11*, 2673.
- [39] S.-S. Chi, X.-G. Qi, Y.-S. Hu, L.-Z. Fan, *Adv. Energy Mater.* **2018**, *8*, 1702764.
- [40] X. Y. Cui, Y. J. Wang, H. D. Wu, X. D. Lin, S. Tang, P. Xu, H. G. Liao, M. S. Zheng, Q. F. Dong, *Adv. Sci.* **2021**, *8*, 2003178.
- [41] J. Zhang, W. Wang, R. Shi, W. Wang, S. Wang, F. Kang, B. Li, *Carbon* **2019**, *155*, 50.
- [42] B. S. Vishnugopi, F. Hao, A. Verma, P. P. Mukherjee, *Phys. Chem. Chem. Phys.* **2020**, *22*, 11286.
- [43] W. Liu, Z. Chen, Z. Zhang, P. Jiang, Y. Chen, E. Paek, Y. Wang, D. Mitlin, *Energy Environ. Sci.* **2021**, *14*, 382.
- [44] F. Hao, B. S. Vishnugopi, H. Wang, P. P. Mukherjee, *Langmuir* **2022**, *38*, 5472.
- [45] B. S. Vishnugopi, F. Hao, A. Verma, L. E. Marbella, V. Viswanathan, P. P. Mukherjee, *ACS Energy Lett.* **2021**, *6*, 2190.
- [46] Q. Shi, Y. Zhong, M. Wu, H. Wang, H. Wang, *Angew. Chem., Int. Ed.* **2018**, *57*, 9069.
- [47] S. Tang, Y. Y. Zhang, X. G. Zhang, J. T. Li, X. Y. Wang, J. W. Yan, D. Y. Wu, M. S. Zheng, Q. F. Dong, B. W. Mao, *Adv. Mater.* **2019**, *31*, 1807495.
- [48] W. Fang, H. Jiang, Y. Zheng, H. Zheng, X. Liang, Y. Sun, C. Chen, H. Xiang, *J. Power Sources* **2020**, *455*, 227956.
- [49] H. Wang, C. Wang, E. Matios, W. Li, *Angew. Chem., Int. Ed.* **2018**, *57*, 7734.
- [50] W. Luo, C. F. Lin, O. Zhao, M. Noked, Y. Zhang, G. W. Rubloff, L. Hu, *Adv. Energy Mater.* **2016**, *7*, 1601526.
- [51] Y. Zhao, L. V. Goncharova, Q. Zhang, P. Kaghazchi, Q. Sun, A. Lushington, B. Wang, R. Li, X. Sun, *Nano Lett.* **2017**, *17*, 5653.
- [52] S. Choudhury, S. Wei, Y. Ozhabes, D. Gunceler, M. J. Zschman, Z. Tu, J. H. Shin, P. Nath, A. Agrawal, L. F. Kourkoutis, T. A. Arias, L. A. Archer, *Nat. Commun.* **2017**, *8*, 898.
- [53] H. Tian, H. Shao, Y. Chen, X. Fang, P. Xiong, B. Sun, P. H. L. Notten, G. Wang, *Nano Energy* **2019**, *57*, 692.
- [54] M. Ma, Y. Lu, Z. Yan, J. Chen, *Batteries Supercaps* **2019**, *2*, 663.
- [55] Z. Xu, J. Yang, T. Zhang, L. Sun, Y. Nuli, J. Wang, S. I. Hirano, *Adv. Funct. Mater.* **2019**, *29*, 1901924.
- [56] Q. Li, Z. Zhang, S. Dong, C. Li, X. Ge, Z. Li, J. Ma, L. Yin, *Part. Part. Syst. Character.* **2017**, *34*, 1600115.
- [57] D.-H. Nam, T.-H. Kim, K.-S. Hong, H.-S. Kwon, *ACS Nano* **2014**, *8*, 11824.
- [58] Z. Liu, X.-Y. Yu, X. W. Lou, U. Paik, *Energy Environ. Sci.* **2016**, *9*, 2314.
- [59] Y. Zhu, X. Han, Y. Xu, Y. Liu, S. Zheng, K. Xu, L. Hu, C. Wang, *ACS Nano* **2013**, *7*, 6378.
- [60] Y. Deng, J. Zheng, Q. Zhao, J. Yin, P. Biswal, Y. Hibi, S. Jin, L. A. Archer, *Small* **2022**, *18*, 2203409.
- [61] W. Liu, D. Lin, A. Pei, Y. Cui, *J. Am. Chem. Soc.* **2016**, *138*, 15443.
- [62] Q. Yun, Y. B. He, W. Lv, Y. Zhao, B. Li, F. Kang, Q. H. Yang, *Adv. Mater.* **2016**, *28*, 6932.
- [63] F. Pei, A. Fu, W. Ye, J. Peng, X. Fang, M. S. Wang, N. Zheng, *ACS Nano* **2019**, *13*, 8337.
- [64] X. B. Cheng, T. Z. Hou, R. Zhang, H. J. Peng, C. Z. Zhao, J. Q. Huang, Q. Zhang, *Adv. Mater.* **2016**, *28*, 2888.
- [65] S. Tang, Z. Qiu, X.-Y. Wang, Y. Gu, X.-G. Zhang, W.-W. Wang, J.-W. Yan, M.-S. Zheng, Q.-F. Dong, B.-W. Mao, *Nano Energy* **2018**, *48*, 101.
- [66] Y. Xu, C. Wang, E. Matios, J. Luo, X. Hu, Q. Yue, Y. Kang, W. Li, *Adv. Energy Mater.* **2020**, *10*, 2002308.
- [67] L. Ye, M. Liao, T. Zhao, H. Sun, Y. Zhao, X. Sun, B. Wang, H. Peng, *Angew. Chem., Int. Ed.* **2019**, *58*, 17054.
- [68] X. He, Y. Ni, Y. Li, H. Sun, Y. Lu, H. Li, Z. Yan, K. Zhang, J. Chen, *Adv. Mater.* **2022**, *34*, 2106565.

- [69] N. Mubarak, F. Rehman, M. Ihsan-Ul-Haq, M. Xu, Y. Li, Y. Zhao, Z. Luo, B. Huang, J. K. Kim, *Adv. Energy Mater.* **2022**, *12*, 2103904.
- [70] L. Tao, A. Hu, L. Mu, D. J. Kautz, Z. Xu, Y. Feng, H. Huang, F. Lin, *Adv. Funct. Mater.* **2020**, *31*, 2007556.
- [71] L. Yue, Y. Qi, Y. Niu, S. Bao, M. Xu, *Adv. Energy Mater.* **2021**, *11*, 2102497.
- [72] K. Lee, Y. J. Lee, M. J. Lee, J. Han, J. Lim, K. Ryu, H. Yoon, B. H. Kim, B. J. Kim, S. W. Lee, *Adv. Mater.* **2022**, *34*, 2109767.
- [73] H. Li, H. Zhang, F. Wu, M. Zarrabeitia, D. Geiger, U. Kaiser, A. Varzi, S. Passerini, *Adv. Energy Mater.* **2022**, *12*, 2202293.
- [74] T. Li, J. Sun, S. Gao, B. Xiao, J. Cheng, Y. Zhou, X. Sun, F. Jiang, Z. Yan, S. Xiong, *Adv. Energy Mater.* **2020**, *11*, 2003699.
- [75] Y. Xu, E. Matios, J. Luo, T. Li, X. Lu, S. Jiang, Q. Yue, W. Li, Y. Kang, *Nano Lett.* **2021**, *21*, 816.
- [76] W. Wu, S. Hou, C. Zhang, L. Zhang, *ACS Appl. Mater. Interfaces* **2020**, *12*, 27300.
- [77] Y. Ma, Y. Gu, Y. Yao, H. Jin, X. Zhao, X. Yuan, Y. Lian, P. Qi, R. Shah, Y. Peng, Z. Deng, *J. Mater. Chem. A* **2019**, *7*, 20926.
- [78] Y. Fang, Y. Zhang, K. Zhu, R. Lian, Y. Gao, J. Yin, K. Ye, K. Cheng, J. Yan, G. Wang, Y. Wei, D. Cao, *ACS Nano* **2019**, *13*, 14319.
- [79] P. Liu, H. Yi, S. Zheng, Z. Li, K. Zhu, Z. Sun, T. Jin, L. Jiao, *Adv. Energy Mater.* **2021**, *11*, 2101976.
- [80] W. Liu, P. Liu, D. Mitlin, *Chem. Soc. Rev.* **2020**, *49*, 7284.
- [81] W. Liu, P. Liu, D. Mitlin, *Adv. Energy Mater.* **2020**, *10*, 2002297.
- [82] Y. Wang, Y. Liu, M. Nguyen, J. Cho, N. Katyal, B. S. Vishnugopi, H. Hao, R. Fang, N. Wu, P. Liu, P. P. Mukherjee, J. Nanda, G. Henkelman, J. Watt, D. Mitlin, *Adv. Mater.* **2023**, *35*, 2206762.
- [83] H. Hao, Y. Wang, N. Katyal, G. Yang, H. Dong, P. Liu, S. Hwang, J. Mantha, G. Henkelman, Y. Xu, J. A. Boscoboinik, J. Nanda, D. Mitlin, *Adv. Mater.* **2022**, *34*, 2106572.
- [84] Y. Wang, Y. Hao, L.-C. Xu, Z. Yang, M.-Y. Di, R. Liu, X. Li, *J. Phys. Chem. C* **2019**, *123*, 3988.
- [85] Z. Huang, B. Song, H. Zhang, F. Feng, W. Zhang, K. Lu, Q. Chen, *Adv. Funct. Mater.* **2021**, *31*, 2100666.
- [86] Z. Li, C. Wang, F. Ling, L. Wang, R. Bai, Y. Shao, Q. Chen, H. Yuan, Y. Yu, Y. Tan, *Adv. Mater.* **2022**, *34*, 2204214.
- [87] Y. Wang, Y. Lai, J. Chu, Z. Yan, Y. X. Wang, S. L. Chou, H. K. Liu, S. X. Dou, X. Ai, H. Yang, Y. Cao, *Adv. Mater.* **2021**, *33*, 2100229.
- [88] C. Wu, Y. Lei, L. Simonelli, D. Tonti, A. Black, X. Lu, W. H. Lai, X. Cai, Y. X. Wang, Q. Gu, S. L. Chou, H. K. Liu, G. Wang, S. X. Dou, *Adv. Mater.* **2022**, *34*, 2108363.
- [89] Y. Zhu, Y. Wen, X. Fan, T. Gao, F. Han, C. Luo, S.-C. Liou, C. Wang, *ACS Nano* **2015**, *9*, 3254.
- [90] T. Koketsu, C. Wu, Y. Huang, P. Strasser, *J. Appl. Electrochem.* **2018**, *48*, 1265.
- [91] Y. Li, Y. Zhang, Q. Xu, L. Hu, B. Shen, H. Liu, C. Dai, S. Bao, M. Xu, *ChemSusChem* **2019**, *12*, 1196.
- [92] H. Wang, Z. Tong, R. Yang, Z. Huang, D. Shen, T. Jiao, X. Cui, W. Zhang, Y. Jiang, C. S. Lee, *Adv. Energy Mater.* **2019**, *9*, 1903046.
- [93] J. Zhang, Y. X. Yin, Y. G. Guo, *ACS Appl. Mater. Interfaces* **2015**, *7*, 27838.
- [94] B. D. Adams, J. Zheng, X. Ren, W. Xu, J. G. Zhang, *Adv. Energy Mater.* **2017**, *8*, 1702097.
- [95] A. Bagmut, *Funct. Mater.* **2019**, *26*, 6.
- [96] L. Guo, G. Oskam, A. Radisic, P. M. Hoffmann, P. C. Searson, *J. Phys. D: Appl. Phys.* **2011**, *44*, 443001.
- [97] Y. Wang, H. Dong, N. Katyal, H. Hao, P. Liu, H. Celio, G. Henkelman, J. Watt, D. Mitlin, *Adv. Mater.* **2022**, *34*, 2106005.
- [98] Y. Ma, Q. Wang, L. Liu, S. Yao, W. Wu, Z. Wang, P. Lv, J. Zheng, K. Yu, W. Wei, K. K. Ostrikov, *ChemElectroChem* **2020**, *7*, 1358.
- [99] Z. W. Seh, J. Sun, Y. Sun, Y. Cui, *ACS Cent. Sci.* **2015**, *1*, 449.
- [100] H. Wang, C. Zhu, J. Liu, S. Qi, M. Wu, J. Huang, D. Wu, J. Ma, *Angew. Chem., Int. Ed. Engl.* **2022**, *61*, 202208506.
- [101] M. Xu, Y. Li, M. Ihsan-Ul-Haq, N. Mubarak, Z. Liu, J. Wu, Z. Luo, J. K. Kim, *Energy Storage Mater.* **2022**, *44*, 477.
- [102] J. Xie, L. Liao, Y. Gong, Y. Li, F. Shi, A. Pei, J. Sun, R. Zhang, B. Kong, R. Subbaraman, J. Christensen, Y. Cui, *Sci. Adv.* **2017**, *3*, eaao3170.
- [103] M. He, R. Guo, G. M. Hobold, H. Gao, B. M. Gallant, *Proc. Natl. Acad. Sci. U. S. A.* **2020**, *117*, 73.
- [104] A. F. Voter, in *Radiation Effects in Solids* (Eds: K. E. Sickafus, E. A. Kotomin, B. P. Uberuaga), Springer, New York **2007**, pp. 1–23.
- [105] B. S. Vishnugopi, M. B. Dixit, F. Hao, B. Shyam, J. B. Cook, K. B. Hatzell, P. P. Mukherjee, *Adv. Energy Mater.* **2022**, *12*, 2102825.
- [106] B. S. Vishnugopi, F. Hao, A. Verma, P. P. Mukherjee, *ACS Appl. Mater. Interfaces* **2020**, *12*, 23931.
- [107] X. Zheng, H. Fu, C. Hu, H. Xu, Y. Huang, J. Wen, H. Sun, W. Luo, Y. Huang, *J. Phys. Chem. Lett.* **2019**, *10*, 707.
- [108] J. Chen, Y. Peng, Y. Yin, M. Liu, Z. Fang, Y. Xie, B. Chen, Y. Cao, L. Xing, J. Huang, Y. Wang, X. Dong, Y. Xia, *Energy Environ. Sci.* **2022**, *15*, 3360.